Chemical Engineering Journal 480 (2024) 148140

Contents lists available at ScienceDirect

Chemical Engineering Journal

journal homepage: www.elsevier.com/locate/cej

Antibacterial type-II InP/ZnO quantum dots via multimodal reactive oxygen species

Saad Ullah Khan [a,1], Guncem Ozgun Eren [a,1], Nazli Atac [b,c], Asim Onal [a], Mohammad Haroon Qureshi [b], Francis Korshe Cooper [b,c], Toghrul Almammadov [d,e], Safacan Kolemen [d], Mehmet Sahin [f], Fusun Can [b,c], Sedat Nizamoglu [a,g,*]

[a] Biomedical Science and Engineering, Graduate School of Science and Engineering, Koç University, Istanbul 34450, Türkiye
[b] Department of Medical Microbiology, School of Medicine, Koç University, Istanbul 34450, Türkiye
[c] Koç University-İşbank Center for Infectious Diseases (KUISCID), Koç University, Topkapi, Istanbul 34450, Türkiye
[d] Department of Chemistry, Koç University, Istanbul 34450, Türkiye
[e] University of Zurich, Winterthurerstrasse 190, 8057 Zurich, Switzerland
[f] Department of Nanotechnology Engineering, Abdullah Gul University, Kayseri 38080, Türkiye
[g] Department of Electrical and Electronics Engineering, Koç University, Istanbul 34450, Türkiye

ARTICLE INFO

Keywords:
Quantum dot
Antibacterial
Type-II
InP
Reactive oxygen species
ROS
Pseudomonas aeruginosa
Escherichia coli
ZnO
ZnS

ABSTRACT

The emergence of multidrug-resistant bacteria as a global health threat has necessitated the exploration of alternative treatments to combat bacterial infections. Among these, photocatalytic nanomaterials such as quantum dots (QDs) have shown great promise and type-I QDs have been investigated thus far. In this study, we introduce type-II InP/ZnO core/shell QDs that are ligand-exchanged with a short-chain inorganic sulfide ion (S^{2-}) for antibacterial activity. Interestingly, InP/ZnO QDs simultaneously generate reactive oxygen species (ROS) including hydroxyl ($^{\bullet}OH$) and superoxide ($O_2^{\bullet-}$) radicals, while only $O_2^{\bullet-}$ radicals can be released by the type-I sulfide-capped InP/ZnS QDs. The optimized nanostructure achieved effective inhibition of *Pseudomonas aeruginosa* and *Escherichia coli* bacteria growth to the level of 99.99% and 70.31% under low-intensity green light illumination of 5 mW.cm^{-2}. Our findings highlight the importance of type-II QDs as a new avenue for developing effective antibacterial agents against drug-resistant pathogens.

1. Introduction

Multidrug resistance of bacteria limits the treatment of infections [1]. *Pseudomonas aeruginosa (P. aeruginosa)* can cause infections in the bloodstream infections, pneumonia and wound infections after surgery [2–4]. Additionally, it poses a significant risk for severe health complications, particularly in relation to burn wounds [5]. *Escherichia coli (E. coli)* is the most common cause of urinary tract infections and can cause recurrent infections with fimbrial attachment and biofilm formation on epithelial cells thus lead to failure of antibiotic treatment [6–8]. Bacteria can also acquire resistance to antibiotics through horizontal gene transfer [9]. Hence, the failure of current antibiotics to effectively treat infections highlights the need to seek novel alternatives for infection treatment [4,10].

In recent years, semiconductor photocatalysis has emerged as a promising technique for antimicrobial activity [11–14]. When they are pumped to an excited state, the semiconductor nanocrystals interact with surrounding oxygen compounds and generate reactive oxygen species (ROS) such as singlet oxygen ($^1O_2$), superoxide ($O_2^{\bullet-}$), hydroxyl radical ($^{\bullet}OH$), and hydrogen peroxide (H_2O_2) [15–17]. ROS is naturally produced as a byproduct of normal oxygen metabolism in living cells and acts as mediators of intracellular reactions. Advantageously, an excessive amount of ROS can cause oxidative stress, leading to DNA fragmentation, penetration of ROS into the cell, and further damage to bacteria cell, ultimately resulting in bacterial cell death [18,19].

The use of inorganic quantum dots (QDs) has gained significant attention as a potential solution for combating drug-resistant bacteria. In this regard, cadmium based QDs showed photocatalytic antibacterial

* Corresponding author at: Biomedical Science and Engineering, Graduate School of Science and Engineering, Koç University, Istanbul 34450, Türkiye. Department of Electrical and Electronics Engineering, Koç University, Istanbul 34450, Türkiye.
E-mail address: snizamoglu@ku.edu.tr (S. Nizamoglu).
[1] Equal Contribution.

https://doi.org/10.1016/j.cej.2023.148140
Received 4 September 2023; Received in revised form 24 November 2023; Accepted 15 December 2023
Available online 20 December 2023

activity, which are controlled by composition and size variation of QDs [10,20–25]. However, cadmium content is not preferred for biological applications due to its heavy metal toxicity. In recent years, cadmium-free QDs such as InP and InP/ZnE (E: S or Se) [26–28], ZnO [29], CuInS [30], and $AgBiS_2$ [31] QDs were investigated as alternative materials. All these QDs possess a type-I band alignment where photogenerated electron and hole wavefunctions are confined in the core region. Differently, type-II QDs have staggered band alignment that leads to spatial separation of electron and hole wavefunctions [32,33], and they show high promise for bioimaging, light amplification and LEDs [34–37]. Since the spatial displacement of charge carriers leads to the decreased recombination probability, this can potentially enhance and control ROS generation [38]. However, the potential of cadmium-free type-II QDs on antibacterial activity has not been explored yet.

In this study, we investigated InP/ZnO core/shell QDs with type-II band alignment as a novel antibacterial agent for the first time. Different from the previous InP-based QDs that only release superoxide radicals [26–28], InP/ZnO QDs effectively generated both $O_2^{\bullet-}$ and $^{\bullet}OH$ radicals at the same time due to the type-II band alignment and presence of sulfide (S^{2-}) ligands as hole capturer (Fig. 1(a)). Moreover, we investigated the thickness of the ZnO shell surrounding the InP core QDs in order to maximize ROS generation. InP/ZnO QDs with 1-ZnO shell facilitated significant antibacterial activity against *P. aeruginosa* and *E. coli* with a growth inhibition of 99.99% and 70.31% under low-level green light illumination of 5 $mW.cm^{-2}$. These findings show that type-II QDs hold high promise for future antibacterial coatings.

2. Results and discussion

For the InP/ZnO core/shell synthesis, we followed the procedure, which was initially proposed by Sadeghi *et al.* [39]. We first synthesized InP core QDs by using hot-injection method of tris-(trimethylsilyl) phosphine ($P(TMS)_3$) on indium chloride ($InCl_3$) in the presence of the oleic acid (OA) and oleylamine (OLA) ligands in 1-octadecene (ODE).

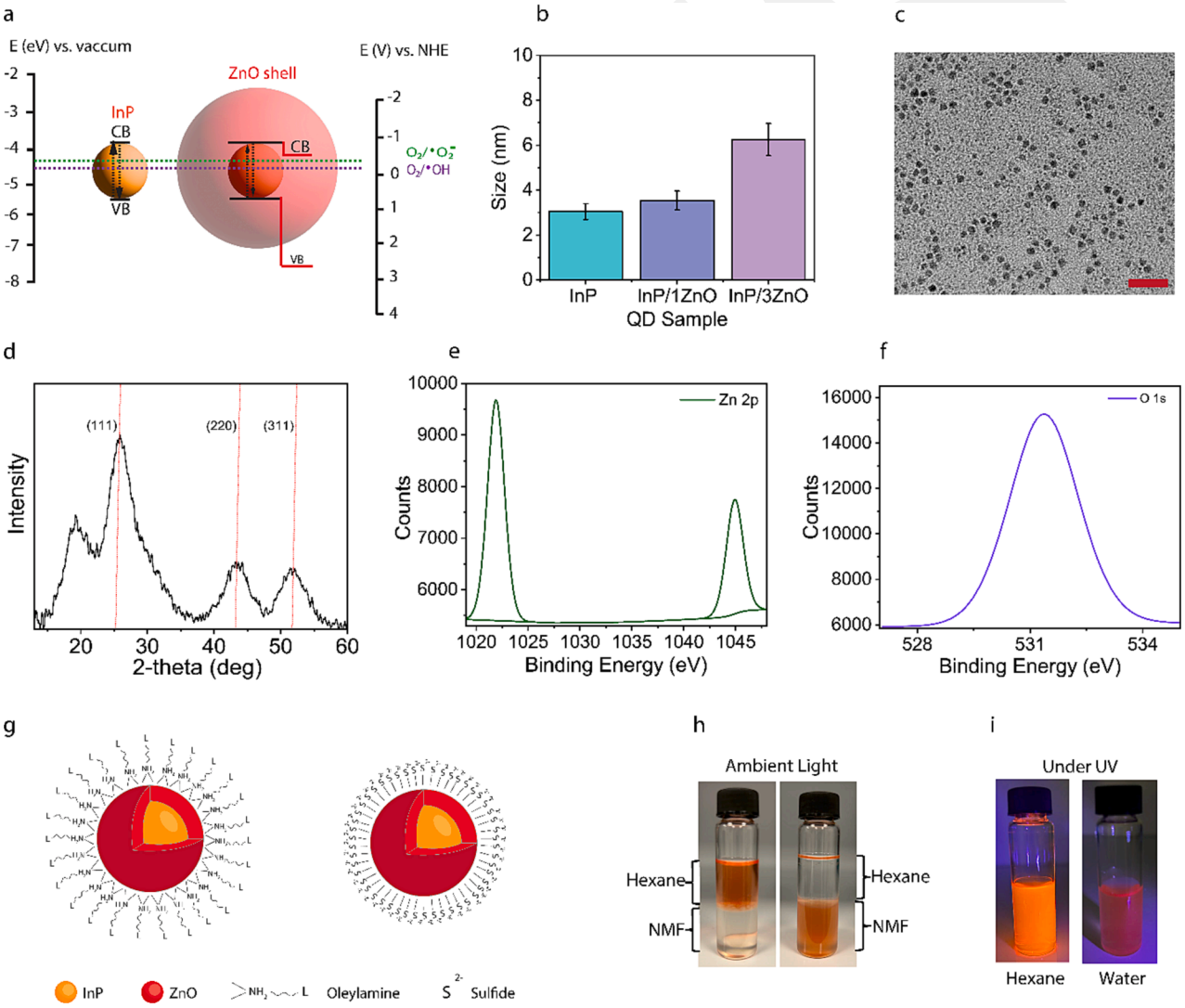

Fig. 1. (a) Schematic illustration of energy band diagram of InP core QDs and InP/ZnO core/shell QDs along with the redox potentials of the superoxide ($O_2^{\bullet-}$) and hydroxyl ($^{\bullet}OH$) radicals. After the photoexcitation process, electron-hole pairs are produced. Charge separation efficiency increases by type-II band alignment and (S^{2-}) ligands. Photogenerated electrons react with O_2 molecules to produce $O_2^{\bullet-}$ and $^{\bullet}OH$ radicals. (b) Mean size of InP core (3.05 nm ± 0.35), InP/1ZnO (3.54 nm ± 0.42), and InP/3ZnO core/shell QDs (6.25 ± 0.73 nm). (c) TEM image of the InP/3ZnO core/shell QDs (6.25 ± 0.73 nm). The scale bar of the TEM images is 20 nm. 200 particles were counted. (d) X-ray diffraction pattern of the InP/ZnO core/shell QDs showing the cubic crystalline structure of InP with the (111), (220), and (311) planes (JCPDS 32–0452), respectively. (e) Zn 2p XPS spectra of InP/ZnO QDs. (f) O 1s XPS spectra of InP/ZnO QDs. (g) Schematic illustration of ligand exchange from OLA to S^{2-} for InP/ZnO QDs. The images of the ligand exchange process from OLA-capped InP/ZnO QDs in hexane (left) to S^{2-} capped InP/ZnO QDs in NMF (h) under ambient and (i) under ultraviolet (UV) light, respectively.

The resulting core size, determined by transmission electron microscopy (TEM), corresponds to 3.05 nm ± 0.35 (Fig. 1(b) and Fig. S1). X-ray diffraction (XRD) analysis confirmed the cubic crystal structure of InP with the (1 1 1), (2 2 0), and (3 1 1) planes (JCPDS 32–0452) (Fig. 1(d)). Additionally, we did not observe any separate XRD peaks of ZnO QDs, which implies that ZnO shell grew on InP core [40]. X-ray photoelectron spectroscopy (XPS) analysis was performed to confirm the elemental surface chemistry of the InP core. In this regard, we identified two distinct peaks at 444.48 eV ($3d_{5/2}$) and 452.02 eV ($3d_{3/2}$) that can be assigned to InP (Fig. S2(a)) [40–42]. Additionally, the dominant doublet at 128.22–129.11 eV ($2p_{3/2}$) was the characteristic peak for InP [40,43], while the doublet in the 132.58–133.47 eV range indicated P atoms in an oxidized medium ($InPO_X$), which is a generally observed phenomena for InP QDs (Fig. S2(b)) [40,44–46].

To form type-II band alignment and to investigate the effect of shell thickness on optical properties of QDs, we grew multiple ZnO shells on InP core structure by using thermal decomposition of zinc acetylacetonate (see methods about the reaction details) [47,48]. The first shell reaction led (i.e., InP/1ZnO) growth up to the size of 3.54 nm ± 0.42 (Fig. 1(b)). After the third-time growth reaction of ZnO shell (i.e., InP/3ZnO), core/shell QD size increased to 6.25 ± 0.73 nm (Fig. 1(b), (c) and Fig. S3). Zn 2p XPS spectrum confirmed that Zn^{2+} was bound to oxygen in the ZnO shell (Fig. 1(e)) [40,49]. Furthermore, the O 1s peak shifted to higher binding energy of 531.37 eV after ZnO coating due to additional oxidation during the shelling procedure (Fig. 1(f)) [41]. Moreover, ZnO shell growth caused shift of In 3d and P 2p peaks towards higher binding energies (Fig. S4(a)-(b)). After the InP/ZnO core/shell QDs synthesis, we performed a ligand exchange process by replacing oleylamine (OLA) with the S^{2-} ligand (i.e., InP/ZnO-S) to trigger reactive oxygen species (ROS) generation in water-based bacterial environment (Fig. 1(g)). The effectiveness of the ligand exchange was confirmed by the successful phase transition of the treated QDs from hexane to N-methyl formamide (NMF) via being stirred at room temperature for 30 mins (Fig. 1(h)-1(i)). Following the ligand-exchange process, the resulting solution was purified by using hexane and acetone. The final precipitate was redissolved in ultrapure water (see experimental studies). The ligand exchange of OLA by S^{2-} ligands was confirmed by Fourier transform infrared (FT-IR) results, which indicate the disappearance of the ligand C-H stretching bands at 2925 and 2855 cm^{-1} (see Fig. S5) [50,51].

We then monitored optoelectronic properties of QDs after shell growth and ligand exchange. For that we did steady-state and time-resolved optical spectroscopy of InP, InP/ZnO and InP/ZnO-S QDs. We observed a red shift in the photoluminescence (PL) spectra following the growth of ZnO shells on top of InP core structure. For example, for 1 ZnO shell the PL peak shifts from 598 nm to 618 nm (≈70 meV) (Fig. 2(a)). In addition, we observed that the red shift in PL emission continues with each subsequent layer of ZnO shell formation (Fig. S6). Moreover, after the 1 ZnO shell growth the time-resolved PL decays increased from 5.1 ns to 13.9 ns (Fig. 2(b)). To investigate the electronic processes, we conducted quantum mechanical calculations employing the effective mass approximation, which was solved via the Poisson and Schrödinger equations in a self-consistent manner using Ben Daniel-Duke boundary conditions. In InP core QDs, both the electron and hole are confined within the same spatial regions. After the subsequent growth of a ZnO shell on the top of InP core QDs, the electron delocalizes toward shell and hole remains confined within the InP core (Fig. 2(d)-(e)). The delocalization of electrons decreases the confinement energy of electrons leading to a spectral red-shift and decreases the electron-hole wavefunction overlap results in slower recombination dynamics, which agree with experimental observations (Fig. 2(a)-(b)).

After ligand exchange with S^{2-}, the PL spectrum (Fig. 2(a)) of InP/1ZnO-S QDs showed a red shift from 618 nm to 646 nm (≈87 meV), which can be attributed to charge transfer (h^+) toward S^{2-} ligands [52,53]. Similarly, red shift around 28 nm and 31 nm in PL emission was observed for InP/2ZnO-S and InP/3ZnO-S core/shell QDs, respectively (Fig. S6). Similarly, we observed a band gap decrease in absorption, which is beneficial for stronger absorption in green spectral region (Fig. S6). Moreover, the exchange of the ligand with S^{2-} led to a substantial decrease in the PLQY values (Fig. 2(c)). Since S^{2-} ligands

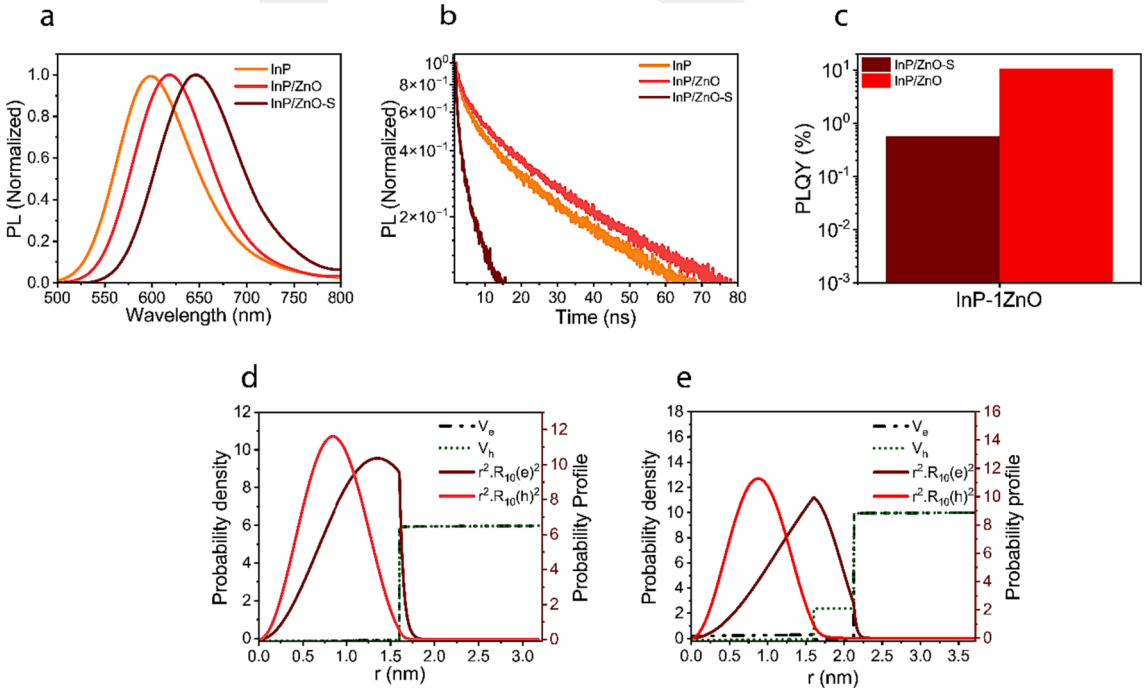

Fig. 2. (a) PL emission spectrum of InP core, InP/1ZnO QDs capped with OLA and S^{2-} (InP/1ZnO-S) ligands. (b) Time-resolved spectroscopy of InP core QDs, InP/1ZnO QDs capped with OLA and S^{2-} (InP/ZnO-S) ligands. (c) PLQY of InP/1ZnO core/shell QDs before and after ligand exchange. Electron (dark red) and hole (red) probability density of (d) InP and (e) InP/1ZnO QDs, respectively. Black and green dotted lines correspond to confinement potential profile for electrons and holes, respectively. (For interpretation of the references to colour in this figure legend, the reader is referred to the web version of this article.)

introduce surface traps and nonradiative recombination centers [52,54,55], the drop of PLQY is expected. In terms of photocatalytic activity, it is important to minimize the radiative recombination rates and direct the photogenerated charges to non-radiative recombination centers of catalytic reactions. Hence, PLQY substantially decreased after S^{2-} ligand exchange because of favorably directing holes to the ligands for ROS generation.

To further investigate the effect of ligand exchange on recombination decay dynamics, we conducted time-resolved photoluminescence spectroscopy (TRPL) analysis (Fig. 2(b)). For OLA-capped InP/1ZnO QDs, the decay of TRPL signal is slow (τ = 13.9 ns). Following the ligand exchange process with S^{2-}, TRPL decay becomes faster (τ = 3.5 ns), due to the transfer of charges toward the surface trap states, which is in line with decreased PLQY (Fig. 2(c)).

To get more insight into antibacterial photocatalytic properties, we investigated ROS generation efficiency of InP/ZnO QDs with multiple ZnO shells. The widely used 2′,7′-dichlorofluorescein diacetate (DCFH-DA) sensor molecule was utilized to detect ROS generation [56]. Upon oxidation by the QDs, DCFH was converted into a fluorescent compound called dichlorofluorescein (DCF), which emits at 525 nm (Fig. S7(a)). To this end, following the ligand exchange process, the intensity of DCF fluorescence for InP/ZnO QDs with multiple ZnO shells was measured. To perform such an experiment, we irradiated the core/shell QDs with green light (λ_{max} = 530 nm) in the photo absorption range of QDs (Fig. S6). Our results presented in Fig. 3(a) show that InP/1ZnO QDs exhibited the highest intensity of ROS in comparison with 2 or 3-ZnO shells. This possibly stems from the fact that while electrons are advantageously delocalized toward QD-electrolyte junction for efficient redox reactions, ZnO shell thickness acts as a potential barrier for holes, which are captured by S^{2-} ligands. When the ZnO shell thickness increases, holes are more confined in core structure and the capturing efficiency of photogenerated holes by S^{2-} ligands decreases. Hence, we conclude that InP/1ZnO-S is the most efficient QD for ROS generation, which we used for the following studies.

Since all generated ROS are sensitive to DCFH-DA molecule, XTT (sodium 3′-[1-[(phenylamino)carbonyl]-3,4-tetrazolium]-bis(4-methoxy-6-nitro)benzene-sulfonic acid hydrate) [57] was utilized to detect and quantify $O_2^{\bullet-}$ radicals generated by the InP/1ZnO-S QDs. XTT was added at a concentration of 50 μM along with InP/1ZnO-S QDs at a concentration of 0.5 mM. The $O_2^{\bullet-}$ oxidize XTT, which leads to the formation of XTT formazan (Eq.(1)) [58], a water-soluble, orange-colored compound that can be detected spectrophotometrically by monitoring the increase in absorbance at 470 nm. As depicted in Fig. 3(b), the absorption spectrum of XTT at 470 nm was displayed under green light irradiation for every 10 min interval light exposure in the presence of InP/1ZnO-S QDs. The results revealed that the absorption at 470 nm increases with irradiation time, indicating the formation of XTT formazan. In the absence of light, no absorption peak was observed, indicating that light is necessary for $O_2^{\bullet-}$ generation. The molar concentration of $O_2^{\bullet-}$ generation was determined as 114 ± 7.34 μM (see supplementary information), which is higher than CdTe QDs [21]. We further characterized singlet oxygen ($^1O_2$) generation by using ABDA (9,10-anthracenediyl-bis(methylene)dimalonic acid) sensor molecule that is widely used for detection and quantification of ($^1O_2$). The solution was irradiated in the presence of QDs and ABDA with 10-minute intervals (Fig. S7(b)) and there is no significant change in the absorbance of ABDA sensor molecules even after 30 min of photoactivation. These results indicate that the generation of $^1O_2$ by InP/1ZnO-S QDs is exceptionally low, suggesting that primarily produces $O_2^{\bullet-}$ [59].

$$XTT + O_2^{\cdot-} \rightarrow O_2 + XTT^{-} \quad (1)$$

To detect other ROS species besides $^1O_2$, we conducted additional experiments by using methyl violet (MV) dye. We utilized isopropanol (IPA) and benzoquinone (BQ) as scavengers for $^{\bullet}OH$ and $O_2^{\bullet-}$ radicals, respectively [60]. We found that the photodegradation of MV was substantially inhibited by both BQ and IPA, indicating that both $O_2^{\bullet-}$ and $^{\bullet}OH$ radicals are generated by InP/1ZnO-S QDs under green light illumination and are responsible for the photodegradation of MV dye (Fig. 3(c)). We also performed a similar experiment by using InP/ZnS QDs with S^{2-} ligands and Fig. S7(c) shows that MV degradation is only inhibited by BQ due to $O_2^{\bullet-}$ radical generation. These analysis techniques confirm that InP/ZnO-S generates $O_2^{\bullet-}$ and $^{\bullet}OH$ radicals due to type-II band alignment and the capturing effect of the S^{2-} ligands [59]. In this regard, we propose a mechanism for the photoactivated ROS generation by InP/ZnO-S QDs based on scavenger experiments. When the photoenergy (hv) exceeds the band gap energy of InP/ZnO-S QDs, electrons (e^-) and holes (h^+) are generated (Eq. (2). The type-II heterostructure promotes the spatial separation of photoexcited electron-hole pairs and the electrons delocalize toward the shell. Additionally, S^{2-} ligand energy level is above the VB of InP [54], thus it improves the charge carrier separation efficiency by capturing photogenerated holes. The electrons react with O_2 molecules to produce superoxide ($O_2^{\bullet-}$) and hydroxyl ($^{\bullet}OH$) from oxygen (O_2) (Eq. (3) &(4) [31]. Even though the hole cannot thermodynamically favor the oxidation of water (Eq. (5) due to the energy level of $H_2O/\ ^{\bullet}OH$ (2.32 V, E(V) vs. reversible hydrogen electrode (RHE)), it can induce antibacterial effect as direct active species [61].

$$InP/ZnO\ QDs + hv \rightarrow e^- + h^+ \quad (2)$$

$$O_2 + e^- \rightarrow O_2^{\bullet-} \quad (3)$$

$$O_2^{\bullet-} + H^+ \rightarrow H^{\bullet}O_2 + OH \quad (4)$$

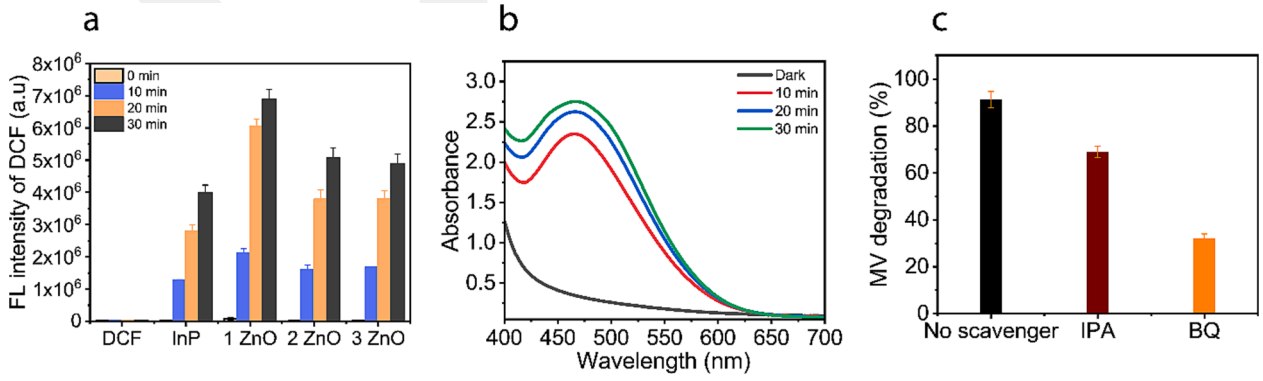

Fig. 3. (a) The fluorescence intensity of DCF molecule indicating relative ROS generation of InP-S core and InP/ZnO-S QDs with multiple ZnO shells after irradiation with green light (λ_{max} = 530 nm). (b) Absorbance spectra of XTT formazan at 470 nm due to generation of $O_2^{\bullet-}$ radical by InP/1ZnO-S QDs at a concentration of 0.5 mM. (c) The photodegradation of MV dye while applying IPA and BQ as scavengers for the detection of $^{\bullet}OH$ and $O_2^{\bullet-}$ radicals, respectively. (For interpretation of the references to colour in this figure legend, the reader is referred to the web version of this article.)

$$H_2O + h^+ \rightarrow H^+ + OH \quad (5)$$

To evaluate the safety of InP/1ZnO-S QDs both for dark and light conditions, we conducted a cytotoxicity assay on Vero E6 cells in Fig. 4 (a). Our results showed that the QDs did not induce significant cytotoxicity in Vero E6 cells at the highest concentration of 125 μM.The cell viability was consistently above 90%, which was comparable to that of the untreated control cells. These findings show that InP/1ZnO-S QDs do not exert harmful effects on Vero E6 cells.

To investigate the antibacterial effect of QDs, we conducted growth inhibition tests under dark and light conditions and included *P. aeruginosa*, *E. coli*, *Staphylococcus epidermidis (S.epidermidis)* and *Enterococcus faecalis (E. faecalis)*. We observed that InP/1ZnO-S QDs did not cause any growth inhibition on *E. faecalis, S.epidermidis*, *E. coli* and

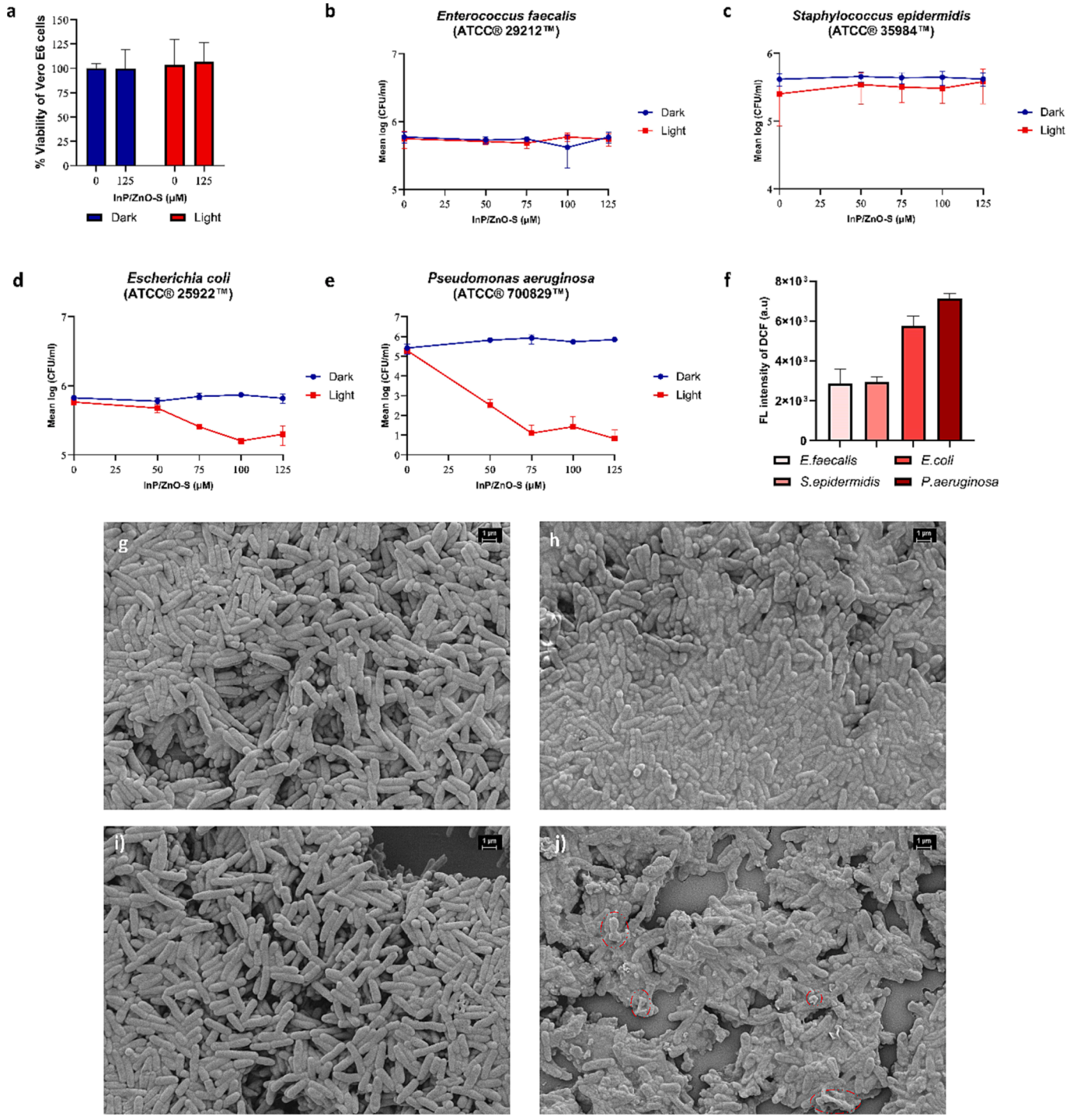

Fig. 4. (a) Cytotoxicity of InP/1ZnO-S QDs under dark condition and low-intensity green light illumination (5 mW cm^{-2}) on Vero E6 cell line at concentration of 125 μM. Viable bacterial counts of (b) *E. faecalis,* (c) *S. epidermidis,* (d) *E. coli* and (e) *P. aeruginosa* with varied concentrations of InP/1ZnO-S QDs (50–125 μM) under dark condition and low-intensity green light illumination (5 mW cm^{-2}). Statistical analysis was performed using One-Way ANOVA test. The bacterial inhibition was considered statistically significant for $p < 0.05$. (f) ROS intensity increase for bacteria in the presence of InP/1ZnO-S QDs under low-intensity green light illumination (5 mW cm^{-2}). SEM image of (g) untreated control bacteria, (h) bacteria incubated with 125 μM InP/1ZnO-S QDs, (i) bacteria under illumination and (j) bacteria incubated with 125 μM InP/1ZnO-S QDs under illumination. The scale bar in SEM images is 1 μm.

P. aeruginosa under dark conditions (Fig. 4(b-e)), respectively [29]. In this regard, we hypothesized that the resulting InP/1ZnO-S QDs do not release free Zn^{+2} ions, which would cause physical disruption of the cell membrane. To confirm our hypothesis, we conducted ICP-MS measurement. The resulting ICP-MS result showed no Zn^{+2} ions releasing from QDs (Fig. S8).

Under green light exposure (λ_{max} = 530 nm) at a low intensity level of 5 $mW.cm^{-2}$, InP/1ZnO-S QDs facilitated a dose-dependent bactericidal effect against *P. aeruginosa* (Fig. 4(e)). 50 μM of QD caused 99.99% growth inhibition (mean CFU/ml reduced from 2.37 x 10^5 to 3.30 x 10^2; p = 0.0231) and the inhibitory effect was sustained with 75, 100 and 125 μM concentrations, mean CFU/ml values being 1.25 x 10^1, 2.67 x 10^1 and 6.67 x 10^0, respectively (p = 0.0228; 0.0108 and 0.0108). Bactericidal effect of InP/1ZnO-S QDs were further confirmed with scanning electron microscopy to observe cellular morphology changes (Fig. 4(g)-(j)). SEM images showed intact cellular morphology for control and QD-exposed groups. When bacteria were exposed to QD plus green light, cell wall condensation and shrinkage was observed in cells marked with red circles. These results suggest that photoactivation of QDs triggers the production of reactive oxygen species, and consequently, this ROS production leads to cell condensation and ultimately culminates in a potent bactericidal effect [62]. These results provide strong evidence for the potential use of InP/1ZnO-S QDs as an effective antimicrobial agent under light activation.

To distinguish between different responses of bacterial species to InP/1ZnO-S QDs under light exposure, we further tested the antibacterial activity against *E. faecalis*, *S. epidermidis* and *E. coli* (Fig.4(b)-(d). No dark toxicity was observed for either of the bacteria. When exposed to green light, *E. coli* showed a lower inhibition rate compared to *P. aeruginosa*. At the lowest concentration of 50 μM QD, 61.81% growth reduction was observed (Mean CFU/ml 4.77 x 10^5) while the growth reduction was enhanced to 76.23% with 75 μM (2.56 x 10^5) and the inhibitory effect sustained for 100 μM QD concentration (70.31% and p < 0.0001). Against gram-positive bacteria (*E. faecalis* and *S. epidermidis*), no inhibition was observed. The growth reduction rate for *E. faecalis* and *S. epidermidis* were 7.78% and 19.56% with their control counts of 5.93 x 10^5 and 4.16 x 10^5, respectively.

In parallel with the growth reduction, 125 μM QD under green light illumination generated the highest levels of ROS in *P. aeruginosa* (Fig.4 (f)). These results suggest that photoactivation of QDs triggers the production of reactive oxygen species and the ROS production leads to species-dependent condensation, which ultimately culminates in a potent bactericidal effect [62]. These results provide strong evidence for the potential use of InP/1ZnO-S QDs against *P. aeruginosa* as an effective antimicrobial agent under light activation.

3. Discussion

In recent years, cadmium-free semiconductor QDs have been widely investigated as effective antibacterial agents against various types of multidrug-resistant bacteria. For instance, ZnO QDs have been found to be highly attractive materials for their ability to inhibit the growth of bacterial microorganisms via the production of ROS under illumination and generation of toxic Zn^{2+} ions. Recently, Gangadoo *et al.* examined the ROS generation of ZnO QDs, and they observed that the resulting ZnO QDs exhibited antimicrobial efficacy of more than 85% against *E. coli* by generating H_2O_2 radicals [29]. However, the poor bandgap tunability of ZnO QDs limits the application of these materials. ZnO is a wide bandgap material (3.1–3.4 eV), thus ZnO-based QDs generally necessitate the use of UV light sources, which are hazardous to mammalian cells [29,63].

Alternatively, InP-based QDs have been attractive material for antibacterial applications due to not only their less toxicity compared to cadmium-based counterparts *in vitro* and *in vivo* [64] but also photo absorption within the visible spectral range [65]. For instance, Levy *et al.*[26] conducted a study to investigate the ligand exchange of type-I InP/ZnS or InP/ZnSe QDs with MPA and their potential effects on multidrug-resistant bacteria (MDR) *E. coli*. To analyze the inhibition of MDR bacteria growth, they performed an extended irradiation exposure of 15 h under low-energy red light. The observed reduction in bacteria growth was attributed to the generation of $O_2^{\bullet-}$ radicals [27]. Similarly, Lee *et al.*[28] employed type-I QDs (InP/ZnS and InP/ZnSe) modified with MPA and investigated their antibacterial effect for multidrug-resistant (MDR) *E.coli* and *S. aureus* by exposing the QDs to blue light irradiation with a highest wavelength of 400 nm. They observed a substantial reduction in bacterial growth followed by the generation of $O_2^{\bullet-}$ radicals.

Different from the previous studies mentioned above, we have shown InP-based QDs with type-II band alignment as a novel and efficient antibacterial agent for the first time. In this regard, we investigated the antibacterial efficacy of the S^{2-} capped InP/ZnO QDs. Considering the literature and control group (i.e., InP/ZnS) experiment together with the cytotoxicity and ICP-MS result (Fig. S8), we conclude that InP/1ZnO-S QDs do not produce free Zn^{+2} ions, which can cause growth inhibition of bacteria [29]. Thanks to type-II band aligning ZnO shell and sulfide ligands, InP/1ZnO-S QDs showed ROS-mediated antibacterial effect by generating $O_2^{\bullet-}$ and $^{\bullet}OH$ radicals compared to type-I InP-based heterostructures, which generate only $O_2^{\bullet-}$.

ROS generation triggers the oxidation of cellular substances such as nucleic acids, proteins, and lipids [66] but the mechanism of action may differ depending both on the gram-negative or gram-positive membrane structure of the bacteria [67] and ROS type [68]. Gram-positive species (i.e., *S. epidermidis* and *E. faecalis*) are more prone to $^1O_2$ while gram-negative bacteria (*E. coli* and *P. aeruginosa*) inhibition is dependent on $O_2^{\bullet-}$ and $^{\bullet}OH$ radicals [69]. In this study, no growth inhibition was observed against *S. epidermidis* and *E. faecalis*, since InP/1ZnO-S QDs did not generate $^1O_2$ as expected. Moreover, we selected green light because some bacterial species *(e.g., P. aeruginosa)* produce endogenous porphyrins such as coproporphyrin III and/or uroporphyrin III, which can be externally activated by blue light [70]. These intra-cellular photosensitive chromophores are prone to blue light and successful eradication of the bacteria was reported both *in vitro* and *in vivo* [70]. Hence, by using green light the antibacterial effect solely induced by QDs were reported (i.e., Fig. 4d & 4e when concentration of QDs is zero under light).

Thick peptidoglycan compartment of gram-positive bacteria limits the ROS action. Since the diffusion length of ROS is under 200 nm, it requires relatively long distance to reach out from QD to the cell wall of gram positive bacteria [71]. Moreover, there are also other endogenous factors that may influence the growth inhibition within the gram-negative bacterial species. Wang et al. reported the higher amount of endogenous porphyrins in *P. aeruginosa* (0.67 ag/CFU) compared to its gram-negative counterpart *E.coli* (0.14 ag/CFU), which is thought to play a role in the higher elimination of *P. aeruginosa* [72]. Furthermore, the structural differences of ROS regulation mechanisms (i.e., via SoxR) within the two gram-negative bacteria might alter ROS response and lead to different growth inhibition rates [73]. In addition, there is none hydrolyzing enzyme of the bacteria to remove $^{\bullet}OH$ radicals [74], thus introduction of them with $O_2^{\bullet-}$ can be advantageous to stress the bacteria through multiple pathways and limit development of resistance against the antibacterial agents.

4. Conclusion

In summary, type-II InP/ZnO-S core/shell QDs can exhibit remarkable photocatalytic activity by simultaneously generating ROS species including $^{\bullet}OH$ and $O_2^{\bullet-}$ radicals. The dual ROS generation was enabled by the ZnO shell growth and sulfur ligand exchange. The highest ROS generation efficiency was recorded with InP/1ZnO-S QDs, which facilitated effective inhibition of multidrug-resistant and biofilm-forming *P. aeruginosa* and *E. coli* under low intensity light illumination. Therefore, we consider that the high-level control of photogenerated charge

carriers via heterojunction and ligand engineering has great potential for future antibacterial agents.

5. Materials and method

5.1. Chemicals

Zinc undecylenate (99%), oleic acid (OA-99%), oleylamine (OAM-99%), octadecene (ODE-90%), indium(III) chloride ($InCl_3$-99%), tris (trimethylsilyl)phosphine ($P(TMS)_3$–95%), zinc acetylacetonate hydrate [$Zn(acac)_2{\cdot}xH_2O$] (99.995%), sodium 3′-[1-[(phenylamino)-carbony]-3,4-tetrazolium]-bis(4-methoxy-6-nitro) benzene-sulfonic acid hydrate (XTT), methyl violet (MV), 2′,7′-dichlorofluorescein diacetate (DCFDA) and sodium sulfide nonahydrate ($Na_2S{\cdot}9H_2O$-98%) were purchased from Sigma-Aldrich. All the chemical handlings were performed in a glovebox under a nitrogen atmosphere. Ligand exchange process was performed in ambient atmosphere.

5.2. $P(TMS)_3$ stock solution preparation

A solution of $P(TMS)_3$ in ODE was prepared with the concentration of 0.1 $mmol.ml^{-1}$ and stored in inert atmosphere at −30 °C.

5.3. Synthesis of InP core QDs

To synthesize InP core quantum dots (QDs), we used zinc undecylenate (43 mg), oleic acid (OA) (32 μL), oleylamine (OLA) (66 μL), and indium chloride ($InCl_3$) (22 mg) mixed in ODE (3 mL). The resulting solution was heated to 120 °C, and the flask was degassed for one hour at the same temperature. Subsequently, the solution was heated to 220 °C under argon (Ar) environment. At this point, 500 μL from phosphine stock solution [$P(TMS)_3$-ODE] was rapidly injected into the mixture and stirred for an additional 30 min. The solution was then cooled to 80 °C, and an aliquot was taken for characterization purposes.

5.4. Synthesis of InP/ZnO core/shell QDs

To prepare the ZnO stock solution, OAM (245 μL), OA (8 μL), and [$Zn(acac)_2{\cdot}xH_2O$] (6.5 mg) were mixed in 1.6 mL ODE solution. This solution was then injected into the as-synthesized InP core solution at 80 °C and heated to 250 °C under the Ar environment. The mixture was stirred for 30 min at the same temperature and then cooled down to room temperature. For additional ZnO shell growth, instead of cooling down to room temperature, the solution was cooled down to 80 °C and same procedure was performed. After InP/ZnO core/shell QDs formation, the crude solution was cooled down to room temperature. Hexane was added into the flask and the resulting crude solution was centrifuged at 11000 rpm for 3 min to remove byproducts. The QD solution was mixed with hexane and ethanol. Then, it was centrifuged at 9000 rpm for 10 min. Precipitation process was repeated two times. The final QDs solution was redispersed in hexane.

5.5. Ligand exchange of InP/ZnO core/shell QDs

Ligand engineering was performed on InP/ZnO quantum dots (QDs) using $Na_2S{\cdot}9H_2O$ as a precursor. The ligand exchange process of a nanomaterial depends on various parameters such as QD concentration, stirring speed, temperature, and solvent polarity. In our experiment, the ligand exchange was carried out at room temperature by mixing InP/ZnO QDs (3–5 mg/mL) in hexane with a $Na_2S{\cdot}9H_2O$ (0.05 M) solution dissolved in the highly polar solvent such as N-methyl-formamide (NMF). Once the QDs were completely transferred from hexane to NMF after 30 mins, the NMF phase was washed twice with hexane to eliminate any residual nonpolar organic species. The NMF phase was then precipitated with acetone. The resulting precipitate was redissolved in water using ultrasound and centrifuged to remove insoluble QDs and impurities. Finally, the resulting colloidal aqueous solution of QDs was stored at 2–6 °C.

5.6. Optical characterization

To comprehensively analyze the properties of QDs, a range of techniques were employed. Steady-state absorbance and photoluminescence measurements were taken using an Edinburgh Instruments (FS5 spectrofluorometer) with an excitation wavelength of 375 nm. Quantum efficiency (i.e., photoluminescence quantum yield - PLQY) was measured using an integrating sphere with an inner diameter of 150 mm. To understand the PL decay dynamics of the QDs, a time-correlated single-photon counting (TCSPC) system (MicroTime 100, Picoquant) was utilized, with a nanosecond pulsed laser ($\lambda = 375$ nm) serving as the excitation source. The fluorescence decay was fitted to a bi-exponential function using Eq.(6).

$$\tau = \frac{A_1\tau_1^2 + A_2\tau_2^2}{A_1\tau_1 + A_2\tau_2} \tag{6}$$

5.7. Structural characterization

To determine the surface composition of the QDs, X-ray photoelectron spectroscopy (XPS) was employed by using a Thermo Scientific K-alpha (Al Kα source) surface analysis tool at ultrahigh vacuum conditions. XPS spectrometer was calibrated by using the C 1s peak at 284.5 eV. For powder X-ray diffraction (XRD) analysis, a Rigaku miniflex XRD instrument with $\lambda_{Cu\ K\alpha} = 1.54$ Å and a scan rate of 5 min^{-1} was utilized. To prepare the samples for XPS and XRD analysis, the QDs were dissolved in hexane and deposited onto a 1 cm x 1 cm silicon wafer. TEM measurements were performed using FEI TALOS F200S TEM 200 kV and Hitachi HT7800 (100 kV). For TEM analysis, samples were deposited as 10 μL of a 1 mM QD in a hexane solution on a copper support grid. For the ICP–MS analysis, an Agilent 7700x inductively coupled plasma-mass spectrometer was used. The powder samples were digested in 10 mL of aqua regia (8 mL of HNO_3 + 2 mL HCl) via a Start D Milestone Microwave Digestion System, and the obtained samples were diluted with a deionized water (18.2 MΩ) by a ratio of 1:3. FT-IR measurement was conducted by using Thermo Scientific iS10 FT-IR.

5.8. ROS detection and quantification

To monitor the generation of reactive oxygen species (ROS), a trap sensor molecule called 2′,7′-dichlorofluorescein diacetate (DCFH-DA) was utilized at a concentration of 10 μM. To convert DCFH-DA to dichlorofluorescin, DCFH-DA in ethanol was reacted with 0.01 N NaOH and allowed to sit at room temperature for 30 min. The hydrolysate was then neutralized with sodium phosphate buffer at pH 7.4. The presence of ROS was detected by an increase in the emission spectrum of DCFH at 525 nm upon oxidation. Both InP/ZnO quantum dots (QDs) and a blank sample were irradiated with green light, and the fluorescence intensity of DCFH at 525 nm was monitored at 0, 10, 20, and 30 min using an Edinburgh Instruments FL-50 spectrofluorometer with excitation at 490 nm. For quantifying superoxide radicals (O_2^-), sodium 3′-[1-[(phenylamino)-carbony]-3,4-tetrazolium]-bis(4-methoxy-6-nitro) benzene-sulfonic acid hydrate (XTT) was used, and the formation of XTT formazan was detected and quantified by the absorbance at 470 nm. For detection and quantification of singlet oxygen ($^1O_2$), ABDA (9,10-anthracenediyl-bis(methylene)dimalonic acid) sensor molecule was used. The molar concentration of each ROS species was determined using Eq. (7).

$$C = \frac{\int_0^T C_0 - C_t dt}{T} \tag{7}$$

where C is the average molar concentration of ROS species, C_o is the

initial concentration of the sensor molecule, C_t is the concentration of the sensor molecule at time t, T is the irradiation time.

The ROS generation mechanism was explored by using methyl violet (MV) dye to test its photodegradation in the presence of InP/ZnO QDs. Isopropanol (IPA) and 1,4 benzoquinone (BQ) were also utilized as scavengers for hydroxyl ($^{\bullet}OH$) and superoxide radicals ($O_2^{\bullet-}$), respectively [75]. The concentration of MV in each light exposure experiment was measured by applying the Beer-Lambert law.

5.9. Quantum mechanical Calculation

To understand the quantum mechanical properties, the Poisson and Schrodinger equations solved self-consistently in the effective mass approximation [76]. In the calculations, the effective mass and dielectric mismatches are considered. In BenDaniel-Duke boundary condition and in the Hartree approximation, the radial Schrödinger equations for electron and hole are given by:

$$\left[-\frac{\hbar^2}{2}\nabla_r\frac{1}{m_e(r)}\nabla_r + V_e(r) - q_e\phi_h(r)\right]R_e(r) = \varepsilon_e R_e(r) \tag{8}$$

$$\left[-\frac{\hbar^2}{2}\nabla_r\frac{1}{m_h(r)}\nabla_r + V_h(r) - q_h\phi_e(r)\right]R_h(r) = \varepsilon_h R_h(r) \tag{9}$$

where, first terms are kinetic energy operators, second terms are confinement potentials for electron and hole, respectively. Third terms are Coulomb interaction terms and with these terms, these two equations are coupled. $\phi_e(r)$ and $\phi_h(r)$ in third terms correspond to electrostatic Coulomb potential or Hartree potential for electron and hole, respectively and $q_{e(h)}$ is the charge of the electron (hole). In Hartree approximation, electron moves in the electrostatic potential of the hole $\phi_h(r)$ and on the other hand, hole moves in the electrostatic potential of the electron $\phi_e(r)$. $\varepsilon_{e(r)}$ and $R_{e(h)}(r)$ correspond to energy eigenvalues and their eigenfunctions for electron (hole). To determine the Hartree potentials of electron and hole, the Poisson equation is solved considering the dielectric mismatch by means of

$$\nabla_r\varepsilon(r)\nabla_r = -\frac{\rho_{e(h)}}{\varepsilon_0} \tag{10}$$

Here, $\varepsilon(r)$ is the dielectric constant of each layer of quantum dot nanocrystal, ε_0 is the dielectric permittivity of the vacuum and $\rho_{e(h)}$ is the charge density of electron (hole). All calculations are carried out fully numerically in real space by matrix diagonalization methods.

5.10. Antibacterial study

The antibacterial activity of InP/ZnO quantum dots was evaluated against *Pseudomonas aeruginosa* ATCC® 700829™, *Escherichia coli* ATCC® 25922™, *Staphylococcus epidermidis* ATCC® 35984™ and *Enterococcus faecalis* ATCC® 29212™ strains. Different concentrations of the quantum dots, ranging from 50 to 125 μM, were tested to assess the dose-dependent antibacterial effect. To perform the assay, overnight bacterial cultures were diluted in 1 x PBS (Biowest) to obtain a final concentration of 10^5 CFU/ml. The diluted cultures were then incubated with the quantum dots for 1 h at 37 °C in 12-well Ibidi chambers. The control group was incubated with PBS only. After the initial incubation, the samples were exposed to a green light source ($\lambda_{max} = 530$ nm) for 4 h. To evaluate the dark antibacterial activity of the quantum dots, a separate set of samples was prepared without light exposure. The bacterial viability was compared to the control group, which did not receive quantum dot treatment or light exposure. To determine the viable bacterial counts, serial dilutions were prepared, and the samples were plated on agar plates. The experiments were performed in triplicate to ensure reproducibility.

ROS generation by QDs under green light illumination was measured via DCFH-DA in bacterial assays with a final concentration of 100 μM DCFH-DA to compare the ROS increase within tested bacteria. Immediately after light exposure, DCFH was added, and fluorescence intensity was measured at 485/538 nm with Biotek spectrophotometer. ROS increase was measured with respect to the untreated controls of each bacterial species.

After the exposure to green light, *P.aeruginosa* samples were prepared for SEM imaging. Briefly, the bacterial pellets were washed with 1x PBS and fixated in 2.5% glutaraldehyde for 1 h. Subsequently, gradual alcohol dehydration was performed by incubating the samples in 50, 70, 80, 90, and 100% ethanol for 10 min each. Following dehydration, 10 μL of the samples were transferred onto glass slides, and the morphologies were compared to untreated bacteria. To obtain high-resolution images, the samples were coated with gold for 45 s and visualized using a scanning electron microscope (SEM) at a magnification of 10,000X. This approach enabled the evaluation of the morphological changes in the bacterial cells following exposure to the quantum dots and green light exposure. The fixation and dehydration steps ensured the preservation of the bacterial structures, and the SEM imaging provided a detailed analysis of the bacterial morphologies.

Cytotoxicity tests for both dark and light conditions were performed on Vero-E6 cell lines, which were grown in high-glucose DMEM supplemented with 10% inactivated Fetal Bovine Serum and 1% Penicillin/Streptomycin/Amphotericin at 37 °C under 5% CO_2. For the dark cytotoxicity assays, the cells were grown to a confluency of 80–90%. Similar to the antibacterial assay, InP/ZnO quantum dots were added to the adhered Vero-E6 cells in a final concentration 125 μM and incubated for 1 h at 37 °C. Following the QD incubation, 4 h light illumination was applied to one culture set in CO_2 incubator (37 °C) and dark culture set was kept similarly at 37 °C without light illumination. After the incubation period, the media were gently removed, and the cells were treated with 0.5 mg/ml MTT for 2 h at 37 °C. After the MTT incubation, 200 μL of DMSO was added to the cells, and the absorbance was measured at 570 nm using a Multiskan GO plate reader.

5.11. Statistical analysis

Viable bacterial counts were compared with One-Way ANOVA test using Graphpad Prism 9. Inhibition caused by QD and / or light exposure were compared to control viable counts. The bacterial inhibition was considered as statistically significant for $p < 0.05$.

CRediT authorship contribution statement

Saad Ullah Khan: Investigation, Methodology, Writing – original draft, Writing – review & editing. **Guncem Ozgun Eren:** Conceptualization, Investigation, Writing – review & editing. **Nazli Atac:** Investigation, Methodology, Writing – review & editing. **Asim Onal:** Data curation, Formal analysis. **Mohammad Haroon Qureshi:** Formal analysis, Methodology. **Francis Korshe Cooper:** Formal analysis, Investigation, Methodology. **Toghrul Almammadov:** Formal analysis, Investigation. **Safacan Kolemen:** Supervision, Writing – review & editing. **Mehmet Sahin:** Software, Supervision, Writing – review & editing. **Fusun Can:** Supervision, Writing – review & editing. **Sedat Nizamoglu:** Conceptualization, Funding acquisition, Supervision, Visualization, Writing – original draft, Writing – review & editing.

Declaration of competing interest

The authors declare the following financial interests/personal relationships which may be considered as potential competing interests: Sedat Nizamoglu reports financial support was provided by European Union's Horizon 2020. Sedat Nizamoglu reports a relationship with European Union's Horizon 2020 that includes: funding grants.

Data availability

Data will be made available on request.

Acknowledgment

This project has received funding from the European Union's Horizon 2020 research and innovation programme under the Marie SKŁODOWSKA-CURIE grant agreement No. 955664 (STIMULUS). The authors thank KUBAM (Koç University Boron and Advanced Materials Application and Research Center, Turkey) for XRD and KUYTAM (Koç University Surface Science and Technology Center, Turkey) for XPS, ICP–MS and SEM imaging, respectively. The authors acknowledge Dr. Suleyman Tekmen from BUMER (Bayburt University Central Research Laboratory, Turkey) for his assistance in TEM characterization. The authors acknowledge Dr. Gülen Esken, Tayfun Barlas and Selma Yalçın from KUISCID (Koç University-İşbank Center for Infectious Diseases, Turkey) for cell culture assays.

Appendix A. Supplementary data

Supplementary data to this article can be found online at https://doi.org/10.1016/j.cej.2023.148140.

References

[1] Z. Khatoon, C.D. McTiernan, E.J. Suuronen, T.-F. Mah, E.I. Alarcon, Bacterial biofilm formation on implantable devices and approaches to its treatment and prevention, Heliyon 4 (2018).
[2] C. Moser, P.Ø. Jensen, K. Thomsen, M. Kolpen, M. Rybtke, A.S. Lauland, H. Trøstrup, T. Tolker-Nielsen, Immune responses to Pseudomonas aeruginosa biofilm infections, Front. Immunol. 12 (2021), 625597.
[3] P. Stewart, T. Bjarnsholt, Risk factors for chronic biofilm-related infection associated with implanted medical devices, Clin. Microbiol. Infect. 26 (2020) 1034–1038.
[4] N. Mesaros, P. Nordmann, P. Plésiat, M. Roussel-Delvallez, J. Van Eldere, Y. Glupczynski, Y. Van Laethem, F. Jacobs, P. Lebecque, A. Malfroot, Pseudomonas aeruginosa: resistance and therapeutic options at the turn of the new millennium, Clin. Microbiol. Infect. 13 (2007) 560–578.
[5] E. Banin, D. Hughes, O.P. Kuipers, Bacterial pathogens, antibiotics and antibiotic resistance, FEMS Microbiol. Rev. 41 (2017) 450–452.
[6] J.R. Brannon, T.L. Dunigan, C.J. Beebout, T. Ross, M.A. Wiebe, W.S. Reynolds, M. Hadjifrangiskou, Invasion of vaginal epithelial cells by uropathogenic Escherichia coli, Nat. Commun. 11 (2020) 2803.
[7] F. Can, O.K. Azap, C. Seref, P. Ispir, H. Arslan, O. Ergonul, Emerging escherichia coli O25b/ST131 clone predicts treatment failure in urinary tract infections, Clin. Infect. Dis. 60 (2015) 523–527.
[8] N. Atac, K. Onbasli, I. Koc, H. Yagci Acar, F. Can, Fimbria targeting superparamagnetic iron oxide nanoparticles enhance the antimicrobial and antibiofilm activity of ciprofloxacin against quinolone-resistant E. coli, J. Microbial. Biotechnol. (2023).
[9] P. Pachori, R. Gothalwal, P. Gandhi, Emergence of antibiotic resistance Pseudomonas aeruginosa in intensive care unit; a critical review, Genes & Diseases 6 (2019) 109–119.
[10] C.M. Courtney, S.M. Goodman, J.A. McDaniel, N.E. Madinger, A. Chatterjee, P. Nagpal, Photoexcited quantum dots for killing multidrug-resistant bacteria, Nat. Mater. 15 (2016) 529–534.
[11] K. Atacan, N. Güy, M. Özacar, Recent advances in photocatalytic coatings for antimicrobial surfaces, Curr. Opin. Chem. Eng. 36 (2022), 100777.
[12] B. Jia, X. Du, W. Wang, Y. Qu, X. Liu, M. Zhao, W. Li, Y.Q. Li, Nanophysical antimicrobial strategies: a rational deployment of nanomaterials and physical stimulations in combating bacterial infections, Adv. Sci. 9 (2022) 2105252.
[13] P. Ganguly, C. Byrne, A. Breen, S.C. Pillai, Antimicrobial activity of photocatalysts: Fundamentals, mechanisms, kinetics and recent advances, Appl Catal B 225 (2018) 51–75.
[14] Z. Shaw, S. Kuriakose, S. Cheeseman, M.D. Dickey, J. Genzer, A.J. Christofferson, R.J. Crawford, C.F. McConville, J. Chapman, V.K. Truong, Antipathogenic properties and applications of low-dimensional materials, Nat. Commun. 12 (2021) 3897.
[15] B. Yang, Y. Chen, J. Shi, Reactive oxygen species (ROS)-based nanomedicine, Chem. Rev. 119 (2019) 4881–4985.
[16] Y. Nosaka, A.Y. Nosaka, Generation and detection of reactive oxygen species in photocatalysis, Chem. Rev. 117 (2017) 11302–11336.
[17] M. Hayyan, M.A. Hashim, I.M. AlNashef, Superoxide ion: generation and chemical implications, Chem. Rev. 116 (2016) 3029–3085.
[18] Q. Cui, J.-Q. Wang, Y.G. Assaraf, L. Ren, P. Gupta, L. Wei, C.R. Ashby Jr, D.-H. Yang, Z.-S. Chen, Modulating ROS to overcome multidrug resistance in cancer, Drug Resist. Updat. 41 (2018) 1–25.
[19] M. Nita, A. Grzybowski, The role of the reactive oxygen species and oxidative stress in the pathomechanism of the age-related ocular diseases and other pathologies of the anterior and posterior eye segments in adults, Oxid. Med. Cell. Longev. (2016) 1–23.
[20] D.F. Stamo, P. Nagpal, A. Chatterjee, Light-activated quantum dot potentiation of antibiotics to treat drug-resistant bacterial biofilms, Nanoscale Advances 3 (2021) 2782–2786.
[21] C.M. Courtney, S.M. Goodman, T.A. Nagy, M. Levy, P. Bhusal, N.E. Madinger, C. S. Detweiler, P. Nagpal, A. Chatterjee, Potentiating antibiotics in drug-resistant clinical isolates via stimuli-activated superoxide generation, Sci. Adv. 3 (2017) e1701776.
[22] M. Levy, C.M. Courtney, P.P. Chowdhury, Y. Ding, E.L. Grey, S.M. Goodman, A. Chatterjee, P. Nagpal, Assessing different reactive oxygen species as potential antibiotics: selectivity of intracellular superoxide generation using quantum dots, ACS Applied Bio Materials 1 (2018) 529–537.
[23] C.R. McCollum, M. Levy, J.R. Bertram, P. Nagpal, A. Chatterjee, Photoexcited quantum dots as efficacious and nontoxic antibiotics in an animal model, ACS Biomater Sci. Eng. 7 (2021) 1863–1875.
[24] T.R. Aunins, K.A. Eller, C.M. Courtney, M. Levy, S.M. Goodman, P. Nagpal, A. Chatterjee, Isolating the Escherichia coli transcriptomic response to superoxide generation from cadmium chalcogenide quantum dots, ACS Biomater Sci. Eng. 5 (2019) 4206–4218.
[25] K.A. Eller, D.F. Stamo, C.R. McCollum, J.K. Campos, M. Levy, P. Nagpal, A. Chatterjee, Photoactivated antibiotics to treat intracellular infection of bacteria, Nanoscale Advances 5 (2023) 1910–1918.
[26] M. Levy, J.R. Bertram, K.A. Eller, A. Chatterjee, P. Nagpal, Near-infrared-light-triggered antimicrobial indium phosphide quantum dots, Angew. Chem. 131 (2019) 11536–11540.
[27] C.R. McCollum, J.R. Bertram, P. Nagpal, A. Chatterjee, Photoactivated indium phosphide quantum dots treat multidrug-resistant bacterial abscesses in vivo, ACS Appl. Mater. Interfaces 13 (2021) 30404–30419.
[28] I. Lee, J. Moon, H. Lee, S. Koh, G.-M. Kim, L. Gauthé, F. Stellacci, Y.S. Huh, P. Kim, D.C. Lee, Photodynamic treatment of multidrug-resistant bacterial infection using indium phosphide quantum dots, Biomaterials Science 10 (2022) 7149–7161.
[29] S. Gangadoo, C. Xu, D. Cozzolino, K. Latham, E. Della Gaspera, J. Chapman, V. K. Truong, Probing nanoscale interactions of antimicrobial zinc oxide quantum dots on bacterial and fungal cell surfaces, Advanced Materials Interfaces 9 (2022) 2101484.
[30] J. Li, X. Wei, Y. Hu, Y. Gao, Y. Zhang, X. Zhang, A fluorescent nanobiocide based on ROS generation for eliminating pathogenic and multidrug-resistant bacteria, J. Mater. Chem. B 9 (2021) 3689–3695.
[31] S. Wen, T. Wu, H. Long, L. Ke, S. Deng, L. Huang, J. Zhang, S. Tan, Mechanism insight into rapid photodriven sterilization based on silver bismuth sulfide quantum dots, ACS Appl. Mater. Interfaces 13 (2021) 21979–21993.
[32] D. Dorfs, T. Franzl, R. Osovsky, M. Brumer, E. Lifshitz, T.A. Klar, A. Eychmüller, Type-I and type-II nanoscale heterostructures based on cdte nanocrystals: a comparative study, small, 4 (2008) 1148-1152.
[33] G.S. Selopal, H. Zhao, Z.M. Wang, F. Rosei, Core/shell quantum dots solar cells, Adv. Funct. Mater. 30 (2020) 1908762.
[34] J.V. Frangioni, S.-W. Kim, S. Ohnishi, S. Kim, M.G. Bawendi, Sentinel lymph node mapping with type-II quantum dots, Applications in Biology, Quantum Dots, 2007, pp. 147–159.
[35] X. Jin, H. Li, S. Huang, X. Gu, H. Shen, D. Li, X. Zhang, Q. Zhang, F. Li, Q. Li, Bright alloy type-II quantum dots and their application to light-emitting diodes, J. Colloid Interface Sci. 510 (2018) 376–383.
[36] J. Nanda, S.A. Ivanov, M. Achermann, I. Bezel, A. Piryatinski, V.I. Klimov, Light amplification in the single-exciton regime using Exciton− Exciton repulsion in type-II nanocrystal quantum dots, J. Phys. Chem. C 111 (2007) 15382–15390.
[37] G. Yang, M. Kazes, D. Raanan, D. Oron, Bright near-infrared to visible upconversion double quantum dots based on a type-II/type-I heterostructure, ACS Photonics 8 (2021) 1909–1916.
[38] Y. Wang, Q. Wang, X. Zhan, F. Wang, M. Safdar, J. He, Visible light driven type II heterostructures and their enhanced photocatalysis properties: a review, Nanoscale 5 (2013) 8326–8339.
[39] S. Sadeghi, H. Bahmani Jalali, R. Melikov, B. Ganesh Kumar, M. Mohammadi Aria, C.W. Ow-Yang, S. Nizamoglu, Stokes-shift-engineered indium phosphide quantum dots for efficient luminescent solar concentrators, ACS Appl. Mater. Interfaces 10 (2018) 12975–12982.
[40] G.O. Eren, S. Sadeghi, H. Bahmani Jalali, M. Ritter, M. Han, I. Baylam, R. Melikov, A. Onal, F. Oz, M. Sahin, Cadmium-free and efficient type-II InP/ZnO/ZnS quantum dots and their application for LEDs, ACS Appl. Mater. Interfaces 13 (2021) 32022–32030.
[41] H. Virieux, M. Le Troedec, A. Cros-Gagneux, W.-S. Ojo, F. Delpech, C. Nayral, H. Martinez, B. Chaudret, InP/ZnS nanocrystals: coupling NMR and XPS for fine surface and interface description, J. Am. Chem. Soc. 134 (2012) 19701–19708.
[42] L. Kazmerski, P. Ireland, P. Sheldon, T. Chu, S. Chu, C. Lin, Comparison of low-temperature oxides on polycrystalline InP by AES, SIMS, and XPS, Journal of Vacuum, Sci. Technol. 17 (1980) 1061–1066.
[43] L. Xi, D.-Y. Cho, A. Besmehn, M. Duchamp, D. Grützmacher, Y.M. Lam, B. E. Kardynał, Effect of zinc incorporation on the performance of red light emitting InP core nanocrystals, Inorg. Chem. 55 (2016) 8381–8386.
[44] M.D. Tessier, E.A. Baquero, D. Dupont, V. Grigel, E. Bladt, S. Bals, Y. Coppel, Z. Hens, C. Nayral, F. Delpech, Interfacial oxidation and photoluminescence of InP-based core/shell quantum dots, Chem. Mater. 30 (2018) 6877–6883.
[45] H.B. Jalali, S. Sadeghi, I.B. Dogru Yuksel, A. Onal, S. Nizamoglu, Past, present and future of indium phosphide quantum dots, Nano Res. 15 (2022) 4468–4489.

[46] Y.-H. Won, O. Cho, T. Kim, D.-Y. Chung, T. Kim, H. Chung, H. Jang, J. Lee, D. Kim, E. Jang, Highly efficient and stable InP/ZnSe/ZnS quantum dot light-emitting diodes, Nature 575 (2019) 634–638.
[47] S. Musić, A. Šarić, S. Popović, Formation of nanosize ZnO particles by thermal decomposition of zinc acetylacetonate monohydrate, Ceram. Int. 36 (2010) 1117–1123.
[48] H. Bahmani Jalali, M. Mohammadi Aria, U.M. Dikbas, S. Sadeghi, B. Ganesh Kumar, M. Sahin, I.H. Kavakli, C.W. Ow-Yang, S. Nizamoglu, Effective neural photostimulation using indium-Based type-II quantum dots, ACS Nano 12 (2018) 8104–8114.
[49] O. Karatum, G.O. Eren, R. Melikov, A. Onal, C.W. Ow-Yang, M. Sahin, S. Nizamoglu, Quantum dot and electron acceptor nano-heterojunction for photo-induced capacitive charge-transfer, Sci. Rep. 11 (2021) 2460.
[50] M.V. Kovalenko, M. Scheele, D.V. Talapin, Colloidal nanocrystals with molecular metal chalcogenide surface ligands, Science 324 (2009) 1417–1420.
[51] A. Nag, M.V. Kovalenko, J.-S. Lee, W. Liu, B. Spokoyny, D.V. Talapin, Metal-free inorganic ligands for colloidal nanocrystals: S2–, HS–, Se2–, HSe–, Te2–, HTe–, TeS32–, OH–, and NH2–as surface ligands, J. Am. Chem. Soc. 133 (2011) 10612–10620.
[52] H.J. Yun, T. Paik, M.E. Edley, J.B. Baxter, C.B. Murray, Enhanced charge transfer kinetics of CdSe quantum dot-sensitized solar cell by inorganic ligand exchange treatments, ACS Appl. Mater. Interfaces 6 (2014) 3721–3728.
[53] A. Jiang, H. Guo, S. Yu, F. Zhang, T. Shuai, Y. Ke, P. Yang, Y. Zhou, Dual charge-accepting engineering modified AgIn5S8/CdS quantum dots for efficient photocatalytic hydrogen evolution overall H2S splitting, Appl Catal B 332 (2023), 122747.
[54] S. Yu, X.-B. Fan, X. Wang, J. Li, Q. Zhang, A. Xia, S. Wei, L.-Z. Wu, Y. Zhou, G. R. Patzke, Efficient photocatalytic hydrogen evolution with ligand engineered all-inorganic InP and InP/ZnS colloidal quantum dots, Nat. Commun. 9 (2018) 4009.
[55] K.V. Vokhmintcev, P.S. Samokhvalov, I. Nabiev, Charge transfer and separation in photoexcited quantum dot-based systems, Nano Today 11 (2016) 189–211.
[56] M.P. Murphy, H. Bayir, V. Belousov, C.J. Chang, K.J. Davies, M.J. Davies, T.P. Dick, T. Finkel, H.J. Forman, Y. Janssen-Heininger, Guidelines for measuring reactive oxygen species and oxidative damage in cells and in vivo, Nature Metabolism 4 (2022) 651–662.
[57] Y. Li, W. Zhang, J. Niu, Y. Chen, Mechanism of photogenerated reactive oxygen species and correlation with the antibacterial properties of engineered metal-oxide nanoparticles, ACS Nano 6 (2012) 5164–5173.
[58] A.A. Boghossian, F. Sen, B.M. Gibbons, S. Sen, S.M. Faltermeier, J.P. Giraldo, C. T. Zhang, J. Zhang, D.A. Heller, M.S. Strano, Application of nanoparticle antioxidants to enable hyperstable chloroplasts for solar energy harvesting, Adv. Energy Mater. 3 (2013) 881–893.
[59] A. Basu, A.J. Misra, M. Behera, S.K. Behera, A.K. Nayak, N.K. Dhal, A. Mishra, B. K. Satpathy, C.S. Lundborg, S.K. Tripathy, Photocatalytic disinfection of extended-spectrum beta-lactamase producing escherichia coli using alumina/ZnO heterostructures, J. Environ. Chem. Eng. 9 (2021), 106334.
[60] X. Zhang, G. Zhang, H. Zhang, X. Liu, J. Shi, H. Shi, X. Yao, P.K. Chu, X. Zhang, A bifunctional hydrogel incorporated with CuS@ MoS2 microspheres for disinfection and improved wound healing, Chem. Eng. J. 382 (2020), 122849.
[61] S. Cheeseman, A.J. Christofferson, R. Kariuki, D. Cozzolino, T. Daeneke, R. J. Crawford, V.K. Truong, J. Chapman, A. Elbourne, Antimicrobial metal nanomaterials: from passive to stimuli-activated applications, Adv. Sci. 7 (2020) 1902913.
[62] Y. Wang, J. Kong, X. Zhang, Y. Liu, Z. Huang, L. Yuan, Y. Zhang, J. Cao, L. Chen, Y. Liu, Plumbagin resurrect colistin susceptible against colistin-resistant Pseudomonas aeruginosa in vitro and in vivo, Front. Microbiol. 13 (2022) 1020652.
[63] W. Xie, S. Zhang, F. Pan, S. Chen, L. Zhong, J. Wang, X. Pei, Nanomaterial-based ROS-mediated strategies for combating bacteria and biofilms, J. Mater. Res. 36 (2021) 822–845.
[64] V. Brunetti, H. Chibli, R. Fiammengo, A. Galeone, M.A. Malvindi, G. Vecchio, R. Cingolani, J.L. Nadeau, P.P. Pompa, InP/ZnS as a safer alternative to CdSe/ZnS core/shell quantum dots: in vitro and in vivo toxicity assessment, Nanoscale 5 (2013) 307–317.
[65] G. Fan, C. Wang, J. Fang, Solution-based synthesis of III–V quantum dots and their applications in gas sensing and bio-imaging, Nano Today 9 (2014) 69–84.
[66] F. Gao, T. Shao, Y. Yu, Y. Xiong, L. Yang, Surface-bound reactive oxygen species generating nanozymes for selective antibacterial action, Nat. Commun. 12 (2021) 745.
[67] X. Wu, M. Yang, J.S. Kim, R. Wang, G. Kim, J. Ha, H. Kim, Y. Cho, K.T. Nam, J. Yoon, Reactivity differences enable ROS for selective ablation of bacteria, Angew. Chem. 134 (2022) e202200808.
[68] X. Hu, H. Zhang, Y. Wang, B.-C. Shiu, J.-H. Lin, S. Zhang, C.-W. Lou, T.-T. Li, Synergistic antibacterial strategy based on photodynamic therapy: progress and perspectives, Chem. Eng. J. 450 (2022), 138129.
[69] L. Huang, Y. Xuan, Y. Koide, T. Zhiyentayev, M. Tanaka, M.R. Hamblin, Type I and Type II mechanisms of antimicrobial photodynamic therapy: an in vitro study on gram-negative and gram-positive bacteria, Lasers Surg. Med. 44 (2012) 490–499.
[70] R.M. Amin, B. Bhayana, M.R. Hamblin, T. Dai, Antimicrobial blue light inactivation of Pseudomonas aeruginosa by photo-excitation of endogenous porphyrins: in vitro and in vivo studies, Lasers Surg. Med. 48 (2016) 562–568.
[71] Y. Liu, H. Zhang, Y. Xu, Quantum dots for pathogenic bacterial monitoring and combating, Adv. Opt. Mater. 11 (2023) 2201826.
[72] Y. Wang, Y. Wang, Y. Wang, C.K. Murray, M.R. Hamblin, D.C. Hooper, T. Dai, Antimicrobial blue light inactivation of pathogenic microbes: state of the art, Drug Resist. Updat. 33 (2017) 1–22.
[73] M. Palma, J. Zurita, J.A. Ferreras, S. Worgall, D.H. Larone, L. Shi, F. Campagne, L. E. Quadri, Pseudomonas aeruginosa SoxR does not conform to the archetypal paradigm for SoxR-dependent regulation of the bacterial oxidative stress adaptive response, Infect. Immun. 73 (2005) 2958–2966.
[74] P.Ø. Jensen, A. Briales, R.P. Brochmann, H. Wang, K.N. Kragh, M. Kolpen, C. Hempel, T. Bjarnsholt, N. Høiby, O. Ciofu, Formation of hydroxyl radicals contributes to the bactericidal activity of ciprofloxacin against Pseudomonas aeruginosa biofilms, Pathogens and Disease 70 (2014) 440–443.
[75] M.R. Shariati, A. Samadi-Maybodi, A.H. Colagar, Dual cocatalyst loaded reverse type-I core/shell quantum dots for photocatalytic antibacterial applications, J. Mater. Chem. A 6 (2018) 20433–20443.
[76] A. Aktürk, M. Sahin, F. Koc, A. Erdinc, A detailed investigation of electronic and optical properties of the exciton, the biexciton and charged excitons in a multi-shell quantum dot nanocrystal, J. Phys. D Appl. Phys. 47 (2014), 285301.